Mechanisms of Intramolecular Rearrangements of Cyclic Siloxycarbenes

Paul G. Loncke and Gilles H. Peslherbe*

Centre for Research in Molecular Modeling and Department of Chemistry & Biochemistry, Concordia University, Montréal, Québec, Canada, H4B 1R6

Received: February 8, 2004

Intramolecular rearrangements of 3-sila-2-oxacyclohexylidene have been investigated using hybrid density functional theory calculations, the quantum theory of atoms in molecules, and the electron localization function. Mechanisms for 1,2-H migration, ring contraction, and decarbonylation have been examined. The mechanism for 1,2-H migration was shown to involve a typical hydride-like shift from the migration origin to the "vacant" carbene p orbital, while ring contraction was found to occur via a concerted pathway involving a front-side nucleophilic attack by the carbene lone pair at silicon as opposed to a stepwise pathway involving an acyl−silyl biradical intermediate. Decarbonylation, on the other hand, was shown to be a stepwise reaction that preferentially occurs via the intermediacy of silacyclopentanone rather than acyl−silyl and alkyl−silyl biradicals. Computed energetics and thermodynamics indicate that 1,2-H migration and ring contraction are considerably more favorable than decarbonylation. Finally, AIM analysis reveals that the changes in molecular structure associated with 1,2-H migration involving a hydride-like shift to the "vacant" carbene p orbital occur via a *conflict mechanism*, whereas those associated with ring contraction (or 1,2-silyl migration) involving front-side nucleophilic attack by the carbene lone pair at silicon occur via a *bifurcation mechanism*. The latter findings further suggest that AIM analysis may be a viable approach to unambiguously distinguish between reaction mechanisms.

Introduction

Cyclic alkoxycarbenes have been known to undergo a number of intramolecular rearrangements, including 1,2-H migration, ring contraction, and decarbonylation.[1−3] Particular attention has been paid to the mechanism of ring contraction not only because it is an intriguing problem but also because it is closely related to the photochemical ring expansion of cycloalkanones.[4−7] Experimental evidence seems to indicate that this reaction occurs via both a concerted mechanism involving an anion-like shift from oxygen to the "vacant" carbene p orbital and a stepwise fragmentation-recombination mechanism involving an acyl−alkyl biradical intermediate.[1−3] Decarbonylation is also believed to involve initial fragmentation to an acyl−alkyl biradical, which thereafter loses carbon monoxide to afford a dialkyl biradical.[1−3] The latter biradical then collapses to the appropriate cycloalkane product.

Recently, it was shown that 1,2-silyl migration and decarbonylation in methoxy(siloxy)carbenes, $MeO\ddot{C}OSiR_3$, occur via intramolecular front-side nucleophilic attack by the carbene lone pair at silicon and by the methoxy oxygen at silicon, respectively.[8−11] In light of these findings, it is of interest to investigate the mechanisms of 1,2-silyl migration (i.e., ring contraction) and decarbonylation, as well as 1,2-H migration, in a cyclic siloxycarbene such as 3-sila-2-oxacyclohexylidene **A** (cf. Scheme 1). Although cyclic siloxycarbenes have been generated by thermolysis and photolysis of acylsilanes, research has focused primarily on their intermolecular reactivity with species such as alkenes, alcohols, acids, aldehydes, and ketones.[12−15] 3,3-Dimethyl-3-sila-2-oxacyclohexylidene has been reported to undergo ring contraction, decarbonylation, and 1,2-H migration,[15] but to our knowledge, the mechanisms of these intramolecular rearrangements have never been investigated, presumably because of the assumption that they are no different from the analogous rearrangements of cyclic alkoxycarbenes.[1−3]

SCHEME 1

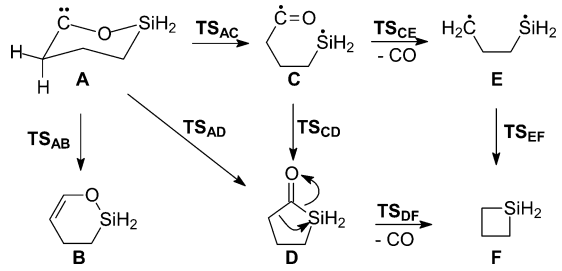

The mechanism for 1,2-H migration in 3-sila-2-oxacyclohexylidene **A** is expected to involve a typical hydride-like shift to the "vacant" carbene p orbital.[16−21] However, the mechanisms for ring contraction and decarbonylation are expected to be a bit more complicated. As illustrated in Scheme 1, ring contraction of **A** could occur via a concerted mechanism or a stepwise mechanism involving the acyl−silyl biradical intermediate **C**. Moreover, the concerted mechanism could involve either an anion-like shift of the silyl group from oxygen to the "vacant" carbene p orbital or front-side nucleophilic attack by the carbene lone pair at silicon. Assuming **A** exists in a chair-like conformation, ring contraction involving an anion-like shift of the silyl group from oxygen to the "vacant" carbene p orbital is expected to be favorable since the relevant frontier orbitals are appropriately aligned (cf. Scheme 2a). Moreover, it is clear from the sketch of the frontier orbitals in Scheme 2a that this mechanism is *symmetry allowed* according to Woodward−Hoffmann rules,[22−27] since interaction between the σ_{O-Si} orbital

* To whom correspondence may be addressed. E-mail: ghp@alcor.concordia.ca.

10.1021/jp0494281 CCC: $27.50
Published on Web 04/29/2004

SCHEME 2

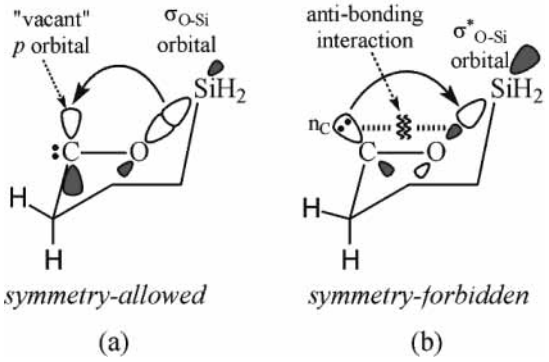

(HOMO) and the "vacant" carbene p orbital (LUMO) leads to a favorable bonding interaction. In contrast, ring contraction involving front-side nucleophilic attack by the carbene lone pair at silicon is not expected to be favorable because of poor alignment of the relevant frontier orbitals (cf. Scheme 2b) and because the "rigid" carbene ring structure may present difficulties in achieving appropriate alignment of the pertinent frontier orbitals. Furthermore, it is evident from the sketch of the frontier orbitals in Scheme 2b that the latter mechanism is *symmetry forbidden*,[22−27] since interaction between the carbene lone-pair n_C orbital (HOMO) and the σ^*_{O-Si} orbital (LUMO) contains a destabilizing antibonding component.[28]

Finally, decarbonylation of 3-sila-2-oxacyclohexylidene **A** could occur via two distinct pathways, both of which are shown in Scheme 1. The first pathway is that involving initial fragmentation to afford the acyl−silyl biradical **C**, followed by loss of carbon monoxide to yield the silabutane biradical **E**, which then collapses to silacyclobutane **F** (cf. Scheme 1). This is similar to the mechanism proposed for decarbonylation of cyclic alkoxycarbenes.[1−3] The second pathway involves initial ring contraction to give silacyclopentanone **D**, followed by decarbonylation to yield **F** (cf. Scheme 1). The mechanism for decarbonylation of **D** in Scheme 1 remotely resembles that proposed by Brook for decarbonylation of methyl triphenylsilylformate involving nucleophilic attack by the methoxy oxygen at silicon.[12]

In this article, we use hybrid density functional theory (DFT) calculations combined with the quantum theory of atoms in molecules (AIM) and the electron localization function (ELF) to investigate the mechanisms of intramolecular rearrangements of 3-sila-2-oxacyclohexylidene **A**. We will first discuss the geometry of carbene **A** and then focus on the mechanisms of 1,2-H migration, ring contraction, and decarbonylation as outlined in Scheme 1.

General Approach and Computational Methods

To shed light on the mechanisms of intramolecular rearrangements of 3-sila-2-oxacyclohexylidene **A**, we performed a series of hybrid DFT calculations using the Becke three-parameter hybrid functional[29,30] with the Lee−Yang−Parr correlation potential[30,31] (B3LYP). Broken-symmetry unrestricted DFT (BS-UDFT) calculations, where the HOMO and LUMO are mixed to destroy α,β spin and spatial symmetries,[32] were used to characterize all open-shell singlet biradical species, while restricted DFT (RDFT) calculations were used for all closed-shell singlet species. BS-UDFT calculations, particularly BS-UB3LYP, have been shown to provide reasonable descriptions of open-shell singlet biradical species.[33] The 6-311+G(2d,p) basis set was found to yield the best compromise between accuracy and performance from preliminary calculations with the 6-31+G(d), 6-311+G(2d,p), cc-pVTZ, and 6-311++G(2df,dp) basis sets. As a matter of fact, B3LYP/cc-pVTZ calculations yielded results very similar to those predicted by B3LYP/6-311+G(2d,p) calculations[8] and so did calculations using the Perdew−Burke−Ernzerhof one-parameter hybrid exchange-correlation functional[34−36] (PBE1PBE) with the 6-311+G(2d,p) basis set. Accordingly, only B3LYP/6-311+G(2d,p) results are reported in this paper, while PBE1PBE/6-311+G(2d,p) results are listed in the Supporting Information section for completeness. All calculations were performed using the Gaussian98 suite of programs.[37] Geometry optimizations were performed using the default Berny algorithm[38] for minimum-energy structures and the eigenvector-following method[39−41] for transition-state structures. Frequency calculations were performed for stationary-point characterizations and to obtain thermochemical data within the rigid rotor-harmonic oscillator approximation using standard statistical mechanics expressions implemented in Gaussian98.[42] Intrinsic reaction coordinate (IRC) calculations were also performed to confirm the identity of the computed transition states. The quantum theory of AIM[43] and the ELF[44−48] were used to probe changes in electronic charge distribution and hence molecular structure. AIM analysis was carried out with the AIMPAC suite of programs[49,50] and AIM2000,[51] while ELF analysis was performed with the TopMod program package.[52] All ELF isosurfaces were plotted with the SciAn program[53] using an ELF isovalue of 0.85. Natural bond orbital (NBO) analysis[54] was also carried out with the NBO program version 3.1[55] available in Gaussian98 to shed some light onto geometric features of **A**.

AIM provides a means of mapping topological properties of the electronic density $\rho(r)$ to Lewis-structure representations of molecules.[43] Gradient vector field analysis partitions the molecular electronic density into regions or *basins*, each belonging to a specific nucleus. The basins can then be integrated to afford properties usually ascribed to atoms. For example, atomic charges can be determined by integration of the electronic density over the basin volume and subtraction of the integrated value from the atomic number. *Critical points* correspond to maxima, minima, and saddle points in $\rho(r)$, i.e., points where the density gradient $\nabla\rho(r)$ is zero. These critical points are classified according to their rank ω and signature σ as (ω,σ), where the rank ω is the number of nonzero curvatures in $\rho(r)$ and the signature σ is the sum of the signs of the curvatures at the critical point. A (3,−3) critical point or *attractor* (nucleus) has three negative curvatures, a (3,−1) or *bond critical point* (BCP) has two negative curvatures and one positive curvature, and a (3,+1) or *ring critical point* (RCP) has one negative curvature and two positive curvatures. The Laplacian of the electronic density $\nabla^2\rho(r)$ identifies regions of local charge concentration ($\nabla^2\rho(r) < 0$) and local charge depletion ($\nabla^2\rho(r) > 0$) in the topology of the electronic density. The outermost quantum shell of an atom where $\nabla^2\rho(r) < 0$ is commonly referred to as the valence-shell charge concentration.[43] The nature of bonding between atoms can be characterized by the value of the electronic density $\rho_b(r)$ and the sign of the Laplacian of the electronic density $\nabla^2\rho_b(r)$ at the BCP. A large $\rho_b(r)$ value together with a large negative $\nabla^2\rho_b(r)$ value are indicative of a sharing of electronic density between atoms and represent a *shared interaction*, characteristic of covalent bonding. In contrast, a low $\rho_b(r)$ value along with a positive $\nabla^2\rho_b(r)$ value indicate that electronic density accumulates in separate atomic basins away from the BCP. The latter features are representative of *closed-shell* interactions typically found in ionic bonding,

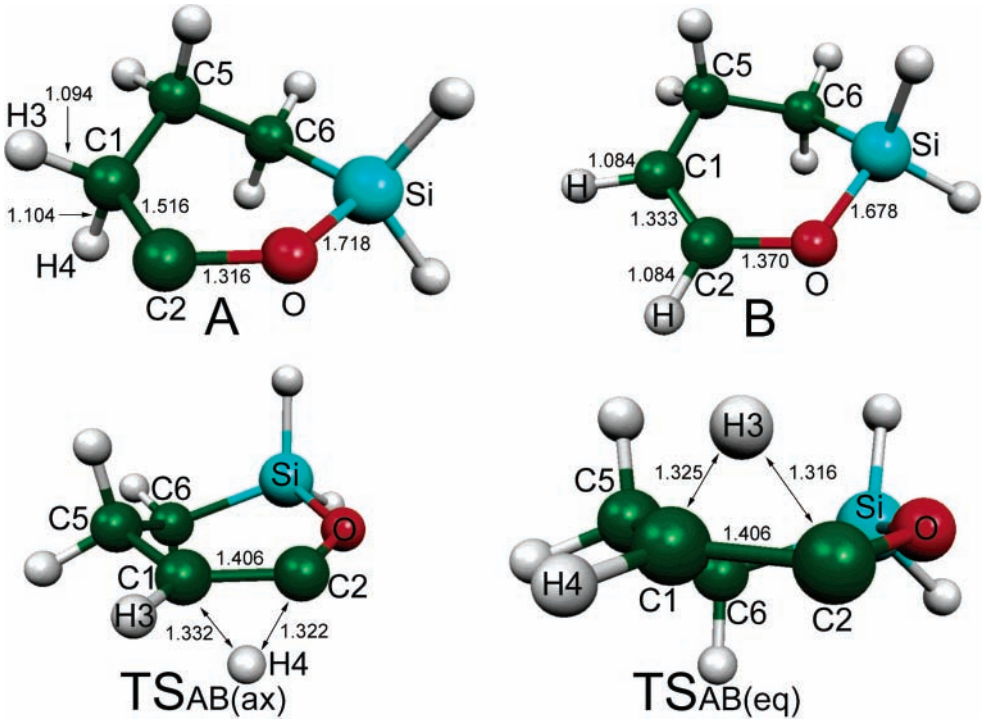

Figure 1. B3LYP/6-311+G(2d,p)-optimized molecular geometries for **A**, **B**, **TS_{AB}(ax)**, and **TS_{AB}(eq)**. Interatomic distances are in Å.

hydrogen bonding, and van der Waals interactions. The *bond ellipticity*, given by $\epsilon = \lambda_1/\lambda_2 - 1$, where the parameters λ_1 and λ_2 are the two negative curvatures at the BCP in the directions perpendicular to the bond path, is a measure of the extent to which charge preferentially accumulates in a given plane along a bond path. For example, an ϵ value of zero reflects the cylindrical symmetry of the charge density at the BCP of a single or triple bond and a value greater than zero is indicative of the elliptical symmetry of the charge density at the BCP for a typical double bond.[43]

The ELF, originally derived by Becke and Edgcombe,[44] provides a means of identifying localized electron pairs in atomic and molecular systems.[44−48] This function, denoted as $\eta(r)$, is given by eq 1 for a single-determinant wave function built from Hartree−Fock or Kohn−Sham orbitals, where $D(r)$ is the excess local kinetic energy density due to *Pauli repulsion* and $D_h(r)$ is the kinetic energy density of an electron gas with the same electronic density (i.e., the Thomas−Fermi kinetic energy density)

$$\eta(r) = \frac{1}{1 + \left(\frac{D(r)}{D_h(r)}\right)^2} \qquad (1)$$

Gradient vector analysis of ELF partitions the molecular electronic density into regions or *basins* of localized electron pairs or *attractors*.[44−48] These basins are classified as *core basins* which surround nuclei with atomic number greater than 2 and *valence basins* in the remaining space. Each valence basin is classified according to its *synaptic order*, which is the number of core basins to which it is attached. Thus, valence basins attached to one, two, three, and more than three core basins are classified as *monosynaptic* (nonbonding), *disynaptic* (bonding), *trisynaptic*, and *polysynaptic* valence basins, respectively. A "disynaptic" basin containing a proton is usually referred to as a *protonated valence basin*. Core and valence basins are usually denoted by $C(X_i)$ and $V(X_i,X_j,...)$, respectively, where X_i and X_j are the atom labels. ELF values fall in the range $0 \le \eta(r) \le 1$. An ELF value of 1.0 corresponds to perfect localization, and a value of 0.5 is equivalent to localization in a homogeneous electron gas (i.e., essentially perfect delocalization). The average basin population $N(\Omega_i)$ is obtained by integration of the one-electron density over the basin volume Ω_i. The population variance $\sigma^2(N,\Omega_i)$ and the relative fluctuation $\lambda(\Omega_i)$, where $\lambda(\Omega_i) = \sigma^2(N,\Omega_i)/N(\Omega_i)$, are measures of basin population delocalization.

Results and Discussion

Molecular Geometry of 3-Sila-2-oxacyclohexylidene. The minimum-energy structure of 3-sila-2-oxacyclohexylidene **A** is shown in Figure 1. It appears that this pseudo half-chair conformer is the only minimum-energy conformer of **A** that exists, presumably because the C2−O bond has significant double-bond character that results in cyclohexene-like characteristics (i.e., half-chair conformation). This double-bond character is reflected in the fact that the C2−O bond in **A** is shorter than it is in 4-sila-3-oxacyclohexene **B** (cf. Figure 1). The double-bond character is also evident from topological properties of the electronic density $\rho(r)$ given in Table 1, where the bond critical point (BCP) electronic density $\rho_b(r)$ for the C2−O bond in **A** is larger than that in **B**. The bond ellipticity ϵ for the C2−O bond in **A** is also greater than zero, consistent with the elliptical symmetry of the BCP electronic density usually associated with double bonds.[43] In comparison, ϵ for the C2−O bond in **B** is essentially zero, reflecting the cylindrical symmetry of the BCP electronic density that is characteristic of single bonds. From the ELF basin properties given in Table 2, it is apparent that the population of the V(C2,O) basin in **A** is larger than it is in **B**, further supporting the notion that the C2−O bond in **A** has double-bond character. In addition, natural bond orbital (NBO) analysis[54] revealed that the most suitable Lewis-structure description of the wave function for **A** is with the C2−O bond as a double bond.

The axial C1−H4 bond of **A** is slightly longer than the equatorial C1−H3 bond as can be seen in Figure 1. Similar observations have been reported for singlet cyclohexylidene

TABLE 1: Topological Properties of the Electronic Density $\rho(r)$ at Pertinent Bond Critical Points for Species Involved in 1,2-H Migration in 3-Sila-2-oxacyclohexylidene[a]

	C1−C2	C1−H3	C1−H4	C2−O	O−Si
			A		
$\rho_b(r)$ (e/Å^3)	1.72	1.86	1.78	2.06	0.80
$\nabla^2\rho_b(r)$ (e/Å^5)	−13.8	−22.1	−20.4	−7.3	13.1
ϵ	0.02	0.03	0.03	0.48	0.01
			TS_{AB}(ax)		
$\rho_b(r)$ (e/Å^3)	2.08	1.91	1.13	1.87	0.87
$\nabla^2\rho_b(r)$ (e/Å^5)	−20.3	−23.5	−2.3	−12.1	15.4
ϵ	0.16	0.03	2.03	0.42	0.04
			TS_{AB}(eq)		
$\rho_b(r)$ (e/Å^3)	2.07	1.15	1.91	1.85	0.88
$\nabla^2\rho_b(r)$ (e/Å^5)	−20.2	−2.5	−23.6	−12.1	15.6
ϵ	0.18	2.07	0.03	0.42	0.04
	C1−C2	C1−H	C2−H	C2−O	O−Si
			B		
$\rho_b(r)$ (e/Å^3)	2.36	1.89	1.95	1.89	0.88
$\nabla^2\rho_b(r)$ (e/Å^5)	−26.3	−23.0	−24.8	−14.0	16.2
ϵ	0.39	0.03	0.05	0.01	0.06

[a] Based on AIM analysis of B3LYP/6-311+G(2d,p) wave functions.

derivatives and have been attributed to stronger hyperconjugative interaction between the axial σ_{C-H} orbital and the vacant carbene *p* orbital.[56,57] On the basis of second-order NBO perturbation-energy analysis, the stabilization energy that arises from axial $\sigma_{C1-H4} \rightarrow p_{C2}$ hyperconjugation is 9.2 kcal/mol while that due to equatorial $\sigma_{C1-H3} \rightarrow p_{C2}$ hyperconjugation is 3.7 kcal/mol. These findings support the notion that the longer axial C1−H4 bond arises from greater hyperconjugative interaction between the axial σ_{C1-H4} orbital and the "vacant" carbene p orbital.

1,2-H Migration. The optimized transition-state geometries, **TS_{AB}(ax)** and **TS_{AB}(eq)**, for 1,2-H migration from the axial and equatorial positions of 3-sila-2-oxacyclohexylidene **A** are shown in Figure 1. For axial 1,2-H migration, the dissociating C1−H4 bond lengthens, while the developing C1−C2 double bond shortens in **TS_{AB}(ax)** relative to **A** (cf. Figure 1). The computed ∠H4C1C2O dihedral angle of 106.1° in **TS_{AB}(ax)** suggests that axial H4 migration occurs essentially perpendicular to the C1C2O carbene valence plane. Simultaneously, the nonmigrating equatorial H3 atom moves into the carbene valence plane, as indicated by the ∠H3C1C2O dihedral angle of 175.0°. Similarly, for equatorial 1,2-H migration, the dissociating C1−H3 bond lengthens, while the developing C1−C2 double bond shortens in **TS_{AB}(eq)** relative to **A** (cf. Figure 1). The calculated ∠H3C1C2O dihedral angle of 104.5° indicates that the equatorial H3 atom migrates perpendicular to the carbene valence plane, while the nonmigrating axial H4 atom becomes coplanar with the carbene valence plane, as reflected in the calculated ∠H4C1C2O dihedral angles of 177.0°. These observations suggest that both axial and equatorial 1,2-H migrations involve hydride-like shifts from the C1 atom to the "vacant" carbene C2 p orbital, perpendicular to the carbene valence plane. The coplanarity of the nonmigrating H3 and H4 atoms with the carbene valence plane in **TS_{AB}(ax)** and **TS_{AB}(eq)**, respectively, is consistent with the development of partial cation-like character at C1 and/or ultimately C1−C2 double-bond formation.

The axial C1−H4 and equatorial C1−H3 bond dissociation in **TS_{AB}(ax)** and **TS_{AB}(eq)**, respectively, is also reflected in topological properties of the electronic density given in Table 1; $\rho_b(r)$ decreases for the C1−H4 and C1−H3 bonds in **TS_{AB}(ax)** and **TS_{AB}(eq)**, respectively, relative to **A**. Values of

TABLE 2: Average Basin Population $N(\Omega_i)$, Relative Fluctuation $\lambda(\Omega_i)$ and %Cross-exchange Contribution for A, TS_{AB}(ax), TS_{AB}(eq) and B[a]

basin	$N(\Omega_i)$	$\lambda(\Omega_i)$	% cross-exchange contribution[b]
		A	
V(C1,C2)	2.03	0.50	V(C2) 9.5; V(C1,H3) 8.0; V(C1,H4) 8.5; V(C1,C5) 6.5
V(C1,H3)	1.98	0.34	V(C1,H4) 9.6; V(C1,C2) 7.0; V(C1,C5) 8.0; V(C2) 2.0
V(C1,H4)	1.94	0.35	V(C1,H3) 9.8; V(C1,C2) 7.3; V(C1,C5) 8.8; V(C2) 2.1
V(C2)	2.23	0.34	V(C1,C2) 8.5; V(C2,O) 6.3; V(O) 5.8
V(C2,O)	1.76	0.58	V(C1,C2) 8.5; V(C2) 8.0; V(O) 24.0; V(O,Si) 12.6
V(O)	3.53	0.40	V(C2,O) 11.9; V(O,Si) 15.0; V(C2) 3.7
V(O,Si)	2.24	0.52	V(O) 23.8; V(C2,O) 9.9; V(C6,Si) 2.2
		TS_{AB}(ax)	
V(C1,C2)	2.26	0.50	V(C2) 9.3; V(C1,H3) 7.6; V(C1,H4,C2) 10.7
V(C1,H3)	2.08	0.32	V(C1,C2) 8.3; V(C1,C5) 7.3; V(C1,H4,C2) 6.8
V(C1,H4C2)	1.58	0.52	V(C2) 13.4; V(C1,H3) 8.9; V(C1,C2) 15.3; V(C1,C5) 5.9
V(C2)	2.14	0.42	V(C1,C2) 9.8; V(C1,H4,C2) 9.8; V(O) 5.6; V(C2,O) 5.1
V(C2,O))	1.32	0.64	V(C2) 8.5; V(O) 29.2; V(O,Si) 10.8; V(C1,C2) 6.9
V(O)	4.24	0.36	V(C2,O) 9.0; V(O,Si) 14.0; V(C2) 2.8
V(O,Si)	2.01	0.55	V(O) 29.5; V(C2,O) 7.0
		TS_{AB}(eq)	
V(C1,C2)	2.25	0.50	V(C1,H3,C2) 10.8; V(C1,C5) 6.7; V(C2,O) 3.6; V(C2) 9.4
V(C1,H3,C2)	1.59	0.52	V(C1,H4) 8.9; V(C1,C5) 5.7; V(C1,C2) 15.2; V(C2) 13.3
V(C1,H4)	2.08	0.32	V(C1,H3,C2) 6.8; V(C1,C5) 7.3; V(C1,C2) 8.3; V(C2) 2.4
V(C2)	2.15	0.41	V(C1,H3,C2) 9.7; V(C1,C2) 9.7; V(C2,O) 5.1; V(O) 5.6
V(C2,O)	1.31	0.64	V(C1,C2) 6.2; V(O,Si) 10.8; V(C2) 8.5;V(O) 29.2
V(O)	4.19	0.37	V(O,Si) 14.4; V(C2,O) 9.1; V(C2) 2.9
V(O,Si)	2.08	0.54	V(O) 29.3; V(C2,O) 6.8
		B	
V(C1,H)	2.12	0.32	V_1(C1,C2) 7.7, V_2(C1,C2) 7.7; V(C1,C5) 7.2
V_1(C1,C2)	1.87	0.55	V_2(C1,C2) 14.6; V(C1,H) 8.1; V(C2,H) 8.6; V(C1,C5) 7.0
V_2(C1,C2)	1.85	0.55	V_1(C1,C2) 14.8; V(C1,H) 8.7; V(C2,H) 8.7; V(C1,C5) 7.1
V(C2,H)	2.16	0.30	V_1(C1,C2) 7.0; V_2(C1,C2) 7.4; V(C2,O) 4.2
V(C2,O)	1.42	0.63	V(O) 29.1; V(O,Si) 9.9; V(C2,H) 6.4; V_1(C1,C2) 5.0
V(O)	4.30	0.36	V(C2,O) 9.6; V(O,Si) 13.6, V_1(C1,C2) 1.2; V_2(C1,C2) 1.2
V(O,Si)	1.90	0.56	V(C2,O) 7.7; V(O) 31.7; V(C6,Si) 2.7

[a] Based on ELF analysis of B3LYP/6-311+G(2d,p) wave functions. [b] Contribution of neighboring basins to the total basin population.

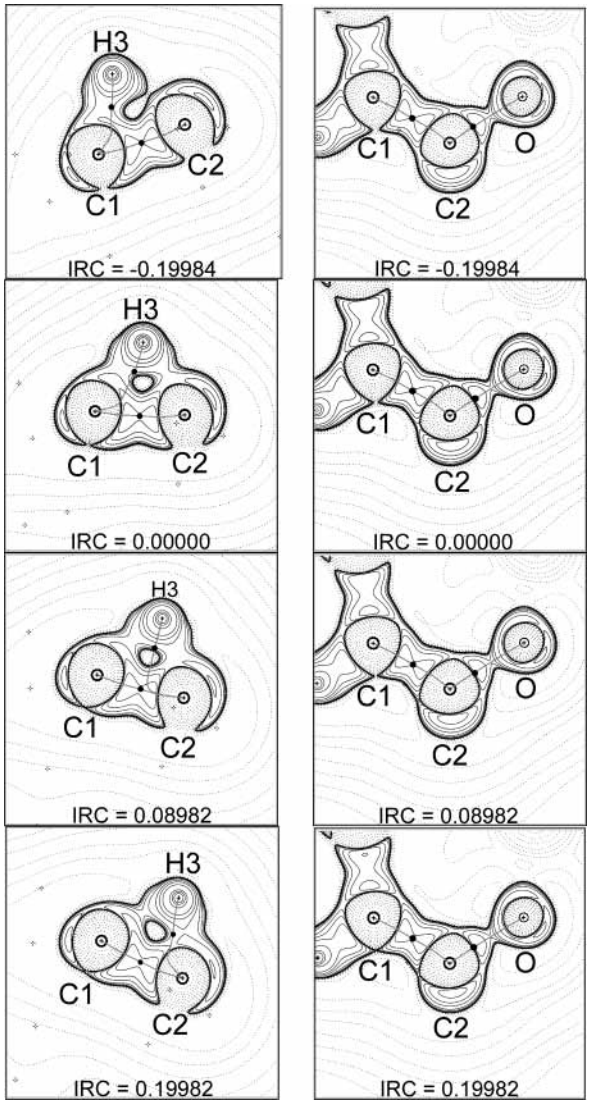

Figure 2. B3LYP/6-311+G(2d,p) contour plots of the Laplacian of the electronic density overlaid by bond paths in the H3C1C2 plane of migration (left) and the C1C2O carbene valence plane (right) at selected IRC values for equatorial 1,2-H migration. The plots for IRC = −0.19984 and 0.00000 amu$^{1/2}$ bohr are in the reactant region of structural stability, while those for IRC = 0.08982 and 0.19982 amu$^{1/2}$ bohr are in the product region of structural stability. Solid and broken contours represent regions of charge concentration and charge depletion, respectively, while solid round dots identify positions of BCPs. Note that some bond paths have deviated out-of-plane.

ϵ also increase dramatically for the C1−H4 bond in **TS$_{AB}$(ax)** and the C1−H3 bond in **TS$_{AB}$(eq)**, consistent with the structural instability of these dissociating bonds.[43] On the other hand, $\rho_b(r)$, as well as ϵ, for the C1−C2 bond increases appreciably in **TS$_{AB}$(ax)** and **TS$_{AB}$(eq)** relative to **A**, indicative of the incipient double-bond formation.

Figure 2 displays contour plots of the Laplacian of the electronic density overlaid by bonds or *bond paths* in the H3C1C2 migration plane and the C1C2O carbene valence plane at selected points along the reaction path for equatorial 1,2-H migration. Negative IRC values correspond to the reactant side of the reaction path, positive IRC values correspond to the product side of the reaction path, and an IRC value of zero represents the transition state. It can be seen that the bond path from H3 terminates at C1 for IRC = −0.19984 and 0.00000 amu$^{1/2}$ bohr, while it terminates at C2 for IRC = 0.08982 and 0.19982 amu$^{1/2}$ bohr, while the region of charge concentration corresponding to the carbene C2 lone pair is essentially identical for all four IRC points (cf. Figure 2). In other words, the carbene C2 lone pair remains intact while the bond path from H3 switches from C1 to C2, which is consistent with a hydride-like shift from C1 to the "vacant" carbene p orbital on C2.

The changes in electronic charge distribution during equatorial 1,2-H migration result in two regions of *structural stability* (i.e., structures that persist for several geometric configurations along the reaction path) corresponding to a *reactant region* and a *product region* (cf. Figure 2). The plots for IRC = −0.19984 and 0.00000 amu$^{1/2}$ bohr, where the bond path from H3 terminates at C1, are in the reactant region of structural stability, while those for IRC = 0.08982 and 0.19982 amu$^{1/2}$ bohr, where the bond path from H3 terminates at C2, are in the product region of structural stability. At some point between IRC = 0.00000 and 0.08982 amu$^{1/2}$ bohr, the bond path from H3 terminates at the C1−C2 BCP. This arrangement of bond paths corresponds to a unique and unstable structure that is transitional between C1−H3 bond dissociation and C2−H3 bond formation. Since the C1 and C2 atoms are in essence competing for the bond path from H3, this arrangement of bond paths is referred to as a *conflict structure*,[43] and the changes in molecular structure are said to occur via a *conflict mechanism*.[43] Thus, it appears that the changes in molecular structure that accompany 1,2-H migration involving a hydride-like shift from C1 to the "vacant" carbene p orbital on C2 occur via a conflict mechanism.

ELF isosurfaces for **A**, **TS$_{AB}$(ax)**, **TS$_{AB}$(eq)**, and **B** are shown in Figure 3, and corresponding ELF basin properties are given in Table 2. For axial 1,2-H migration, it is apparent that the V(C1,H4) protonated valence basin in **A** develops into the V(C1,H4,C2) trisynaptic valence basin in **TS$_{AB}$(ax)**, while the V(C2) lone-pair valence basin remains unchanged (cf. Figure 3). Likewise, for equatorial 1,2-H migration, the V(C1,H3) protonated valence basin in **A** turns into the V(C1,H3,C2) trisynaptic valence basin in **TS$_{AB}$(eq)**, while the V(C2) lone-pair valence basin remains essentially unaltered (cf. Figure 3). These observations are in keeping with a hydride-like shift to the "vacant" carbene p orbital. In addition, the V(C1,C2) basin population increases in **TS$_{AB}$(ax)** and **TS$_{AB}$(eq)** relative to **A**, in accord with imminent C1−C2 double-bond formation (cf. Table 2). Formation of the V(C1,H4,C2) and V(C1,H3,C2) trisynaptic basins, which in essence corresponds to three-center two-electron bonds, suggests that the migrating H4 and H3 atoms in **TS$_{AB}$(ax)** and **TS$_{AB}$(eq)**, respectively, share their bonding electrons with both the C1 and C2 atoms. We note that the populations of the V(C1,H4,C2) and V(C1,H3,C2) basins in **TS$_{AB}$(ax)** and **TS$_{AB}$(eq)** are smaller than those of the parent V(C1,H4) and V(C1,H3) basins in **A**, which is most likely due to greater population delocalization, as evident from the larger relative fluctuation $\lambda(\Omega_i)$ values given in Table 2.

Thermochemical data for **A**, **B**, **TS$_{AB}$(ax)**, and **TS$_{AB}$(eq)** can be found in Table 3, and a relative Gibbs free-energy profile is shown in Figure 4. It is apparent that axial 1,2-H migration via **TS$_{AB}$(ax)** is slightly more favorable than equatorial 1,2-H migration via **TS$_{AB}$(eq)**. Thus, even though axial $\sigma_{C1-H4} \rightarrow p_{C2}$ hyperconjugation is noticeably greater than equatorial $\sigma_{C1-H3} \rightarrow p_{C2}$ hyperconjugation according to second-order NBO perturbation-energy analysis, only a slight preference for axial 1,2-H migration is observed. This is consistent with the experimental observation that 1,2-H migrations in 4-*tert*-butyl-2-substituted-cyclohexylidenes occur with little axial preference,[58,59] a finding that is further supported by theoretical calculations of 1,2-H migrations in cyclohexylidenes.[57,60]

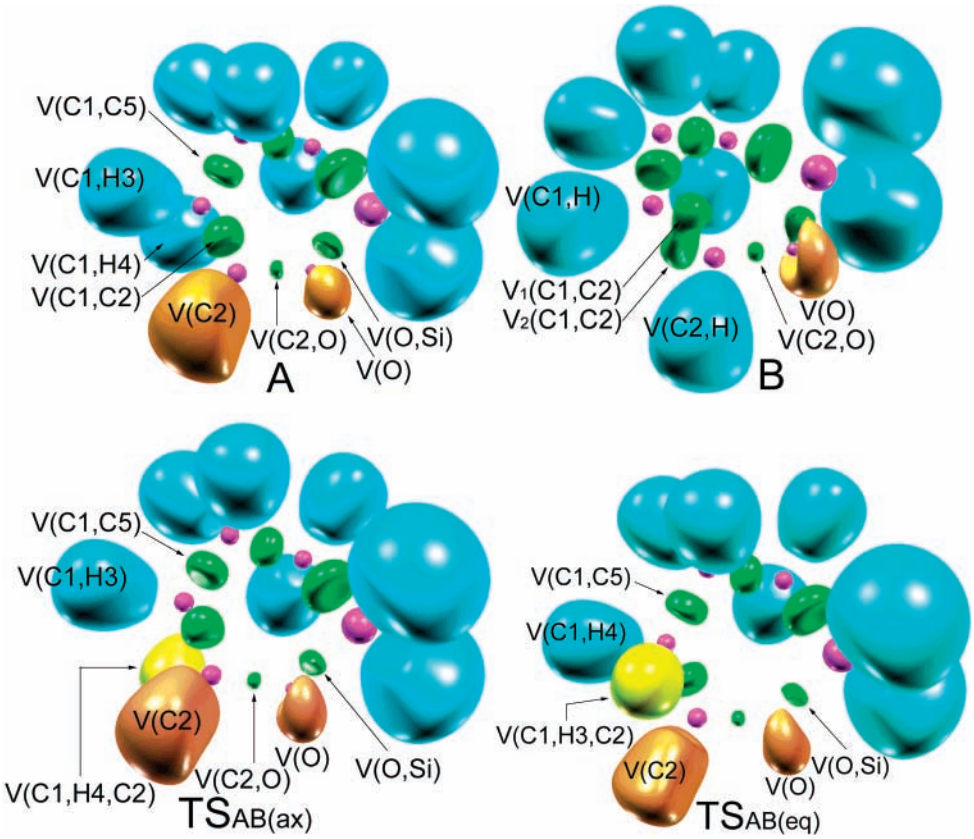

Figure 3. B3LYP/6-311+G(2d,p) ELF isosurfaces for **A**, **B**, **TS_{AB}(ax)**, and **TS_{AB}(eq)**. The basins shown are core basins (purple), protonated valence basins (blue), disynaptic valence basins (green), trisynaptic valence basins (yellow), and lone-pair valence basins (orange).

TABLE 3: Relative B3LYP/6-311+G(2d,p) Zero Point Energy Corrected Electronic Energies, Enthalpies, and Gibbs Free Energies for Intramolecular Rearrangements of 3-Sila-2-oxacyclohexylidene A[a]

	ΔE	ΔH	ΔG
A	0.0	0.0	0.0
TS_{AB}(ax)	16.4	16.2	16.6
TS_{AB}(eq)	17.3	17.1	17.3
B	−50.7	−50.9	−50.6
TS_{AC}	27.8	28.2	27.0
C	27.7	28.6	25.8
TS_{AD}	18.7	18.4	19.2
TS_{CD}	28.5	29.2	27.0
D	−32.5	−32.4	−32.6
TS_{CE}	41.2	42.6	38.5
TS_{DF}	18.7	19.1	18.0
E + CO	35.7	38.1	23.2
TS_{EF} + CO	35.8	37.7	24.5
F + CO	−20.3	−19.6	−30.9

[a] Energies, enthalpies, and free energies are given in kcal/mol, at 298.15 K and 1.0 atm, relative to **A**. The zero point energy corrected electronic energy, enthalpy, and Gibbs free energy values for **A** are −521.887101, −521.879593, and −521.917353 Hartree, respectively.

Ring Contraction. As mentioned earlier, the mechanism for ring contraction of 3-sila-2-oxacyclohexylidene **A** could be concerted or stepwise, as outlined in Scheme 1. Let us first consider the mechanism for ring contraction via the concerted pathway. Computed geometric structures of the transition state **TS_{AD}** and product silacyclopentanone **D** are shown in Figure 5. Relative to **A** (cf. Figure 1), the O−Si bond lengthens and the C2−O bond shortens in **TS_{AD}**, consistent with O−Si bond dissociation and C2−O double-bond formation. The calculated ∠SiOC2C1 dihedral angles of 114.7° for **TS_{AD}** suggest that the O−Si bond is essentially aligned with the "vacant" carbene p orbital (i.e., perpendicular to the C1C2O carbene valence plane), which seems to be in accord with an anion-like shift of the silyl group from oxygen to the carbene carbon C2. However, as will be discussed below, our AIM and ELF analyses show that the latter inference is likely erroneous.

Figure 6 contains contour plots of the Laplacian of the electronic density overlaid by bond paths in the C2OSi plane at selected points along the reaction path for ring contraction of **A**. From the sequence of plots in the figure, it can be seen that the region of charge concentration corresponding to the carbene C2 lone pair becomes polarized toward Si as the reaction progresses from the reactant side of the reaction path (negative IRC values) to the product side of the reaction path (positive IRC values). This observation is clearly indicative of nucleophilic attack by the carbene lone pair at silicon, which is in contrast to the above conclusion.

The changes in electronic charge distribution during ring contraction of **A** result in three regions of structural stability corresponding to a reactant region, an intermediate *ring-structure region*, and a product region (cf. Figure 6). The plots for IRC = −1.08707 and 0.00000 amu$^{1/2}$ bohr are in the reactant region of structural stability, while those for IRC = 0.39476 and 0.59321 amu$^{1/2}$ bohr are in the ring-structure and product regions of structural stability, respectively. This sequence of changes in molecular structure is characteristic of a *bifurcation mechanism*.[43] At some point between IRC = 0.00000 and 0.39476 amu$^{1/2}$ bohr, as the C2 and Si nuclei approach each other, a unique and unstable critical point appears in the electronic charge distribution. This critical point, referred to as a *bifurcation catastrophe point*,[43] is a minimum in $\rho(r)$ along the line connecting the C2 and Si nuclei (positive curvature), a maximum along a line perpendicular to the C2OSi plane (negative

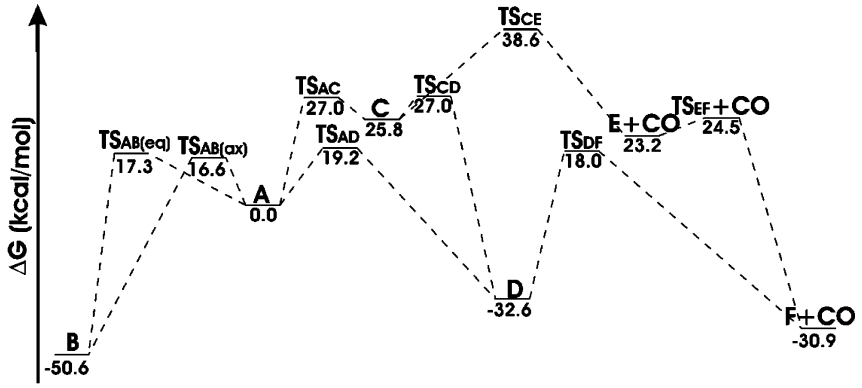

Figure 4. Relative B3LYP/6-311+G(2d,p) Gibbs free-energy profile for intramolecular rearrangements of 3-sila-2-oxacyclohexylidene **A** at 298.15 K and 1.0 atm.

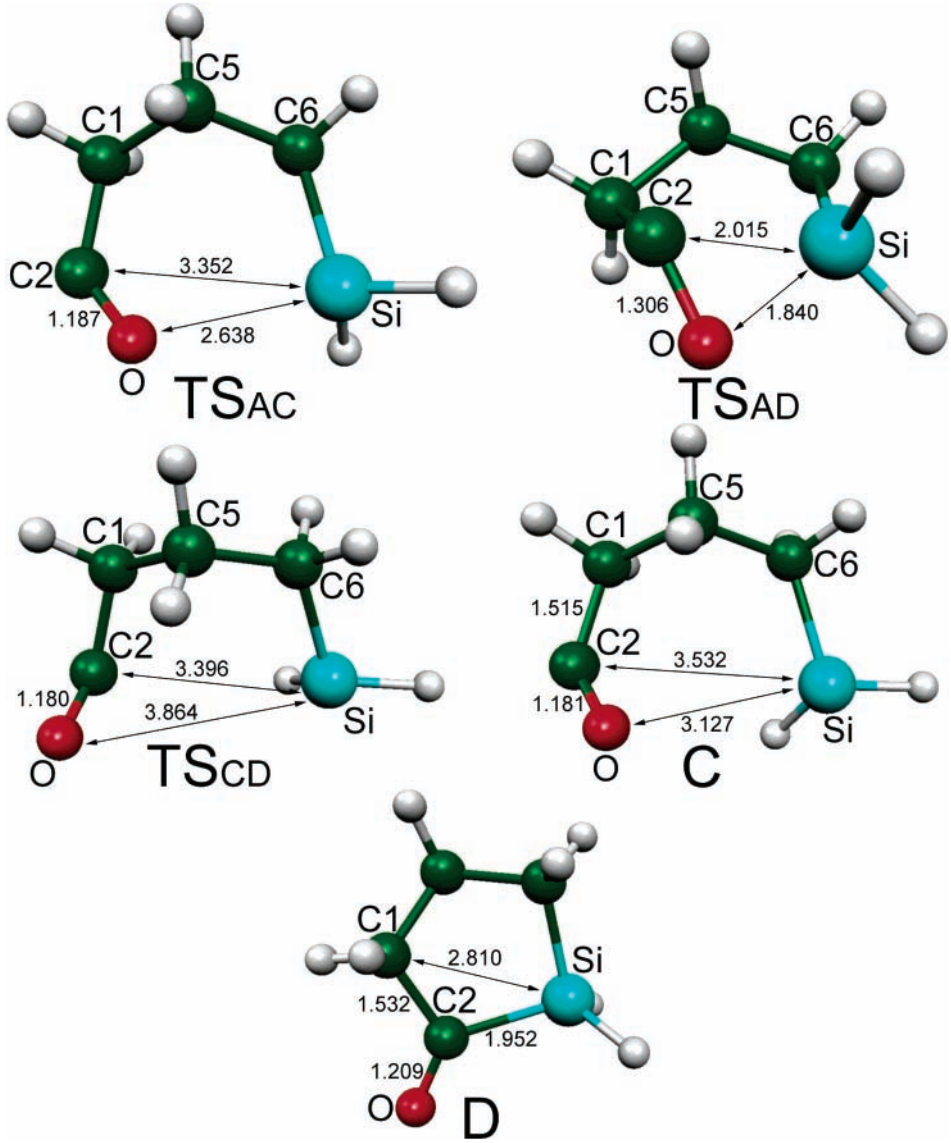

Figure 5. B3LYP/6-311+G(2d,p)-optimized molecular geometries for $\mathbf{TS_{AC}}$, $\mathbf{TS_{AD}}$, $\mathbf{TS_{CD}}$, **C**, and **D**. Interatomic distances are in Å.

curvature), and a point of inflection on a line originating from infinity and terminating at either the C2−O or O−Si BCP (zero curvature). Further motion along the reaction path results in the bifurcation of this unstable critical point into a new C2−Si BCP and C2−O−Si RCP. As motion continues along the reaction path, the RCP migrates towards the dissociating O−Si BCP, and when they eventually coalesce, the system has reached a second bifurcation catastrophe point. Continued motion along the reaction path eventually results in complete annihilation of the O−Si bond path, and the system enters the product region of structural stability. Thus, the changes in molecular structure accompanying the ring contraction of **A** involving front-side nucleophilic attack by the carbene lone pair at silicon occur via a bifurcation mechanism.

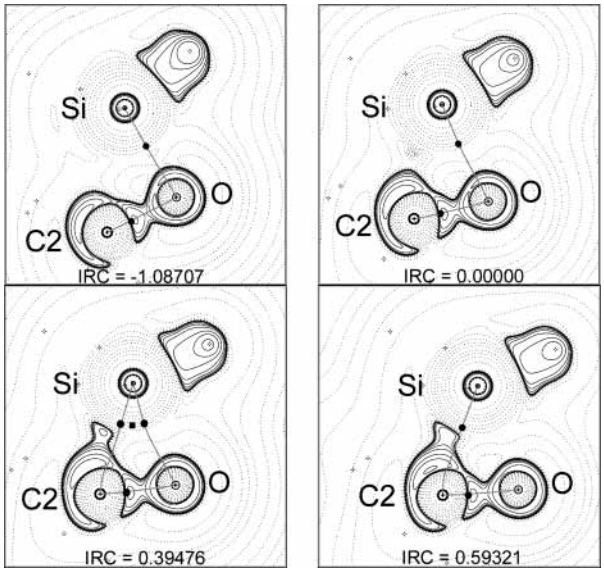

Figure 6. B3LYP/6-311+G(2d,p) contour plots of the Laplacian of the electronic density overlaid by bond paths in the C2OSi plane at selected IRC values for ring contraction of **A**. Plots for IRC = −1.08707 and 0.00000 amu$^{1/2}$ bohr are in the reactant region of structural stability, while those for IRC = 0.39476 and 0.59321 amu$^{1/2}$ bohr are in the ring-structure and product regions of structural stability, respectively. Solid and broken contours represent regions of charge concentration and charge depletion, while solid round and square dots identify positions of BCPs and RCPs. Note that some bond paths have deviated out-of-plane.

From the topological properties of the electronic density given in Table 4, it is evident that $\rho_b(r)$ for the O−Si and C2−O bonds decreases and increases, respectively, in **TS$_{AD}$** relative to **A** (cf. Table 1), consistent with O−Si bond dissociation and C2−O double-bond formation. The large ϵ values for the dissociating O−Si bond and the developing C2−O double bond in **TS$_{AD}$** most likely results from the unsymmetrical distribution of the BCP electronic density due to the developing ring-structure region of structural stability (cf. Figure 6).[43] The large ϵ values for the C2−O bond in **TS$_{AD}$** may also be due to the incipient elliptical symmetry of the BCP electronic density usually associated with double bonds.[43]

ELF isosurfaces for **TS$_{AD}$** and **D** are shown in Figure 7, and corresponding ELF basin properties are collected in Table 5. Close inspection of the ELF isosurfaces reveals that the V(C2) lone-pair basin in **A** (cf. Figure 3) turns into the V(C2,Si) bonding basin in **TS$_{AD}$**, which is clearly indicative of nucleophilic attack by the carbene lone pair at silicon, in accord with the AIM findings above. We also note that the V(O,Si) basin in **A** shifts slightly toward oxygen in **TS$_{AD}$**. As a matter of fact, the V(O,Si) basin is located 0.627 and 0.576 Å away from oxygen in **A** and **TS$_{AD}$**, respectively. This shift in the V(O,Si) basin is consistent with O−Si bond dissociation, since it is known that the bonding valence basin corresponding to a dissociating bond tends to shift toward the more electronegative atom.[46] It is also apparent from the ELF isosurfaces that the V(O,Si) basin in **A** (cf. Figure 3) acquires some lone-pair basin character in **TS$_{AD}$** (cf. Figure 7), as it becomes part of the V1(O)∪V2(O) superbasin of the C2−O carbonyl group in **D**. We note that the V(O,Si) basin population increases in **TS$_{AD}$** (cf. Table 5) relative to **A** (cf. Table 2), most likely due to additional cross-exchange contribution arising from the developing V(C2,Si) basin in **TS$_{AD}$**. Also, the V(C2,O) basin population increases in **TS$_{AD}$** relative to **A**, in keeping with C2−O double-bond formation. The increase in the V(C2,O) basin population in **TS$_{AD}$** relative to **A** may also be partly due to additional cross-exchange contribution from the developing V(C2,Si) basin in **TS$_{AD}$**. Thus, it is quite clear from both AIM and ELF analyses that ring contraction of 3-sila-2-oxacyclohexylidene **A** via the concerted pathway involves front-side nucleophilic attack by the carbene lone pair at silicon.

TABLE 4: Topological Properties of the Electronic Density $\rho(r)$ at Pertinent BCPs for the Species Involved in the Ring Contraction and Decarbonylation of 3-Sila-2-oxacyclohexylidene[a]

	C1−C2	C2−O	O−Si	C2−Si
		TS$_{AC}$		
$\rho_b(r)$ (e/Å^3)	1.64	2.90	0.17	
$\nabla^2\rho_b(r)$ (e/Å^5)	−12.5	0.0	1.0	
ϵ	0.01	0.09	0.02	
		TS$_{AD}$		
$\rho_b(r)$ (e/Å^3)	1.82	2.25	0.59	
$\nabla^2\rho_b(r)$ (e/Å^5)	−15.8	−13.3	8.4	
ϵ	0.02	0.27	0.46	
		C		
$\rho_b(r)$ (e/Å^3)	1.62	2.96	0.06	
$\nabla^2\rho_b(r)$ (e/Å^5)	−12.2	−0.3	0.6	
ϵ	0.01	0.06	0.32	
		TS$_{CD}$		
$\rho_b(r)$ (e/Å^3)	1.59	2.97		
$\nabla^2\rho_b(r)$ (e/Å^5)	−11.6	−0.2		
ϵ	0.01	0.05		
		TS$_{CE}$		
$\rho_b(r)$ (e/Å^3)	0.35	3.28		
$\nabla^2\rho_b(r)$ (e/Å^5)	1.4	2.6		
ϵ	0.03	0.00		
		D		
$\rho_b(r)$ (e/Å^3)	1.65	2.82		0.76
$\nabla^2\rho_b(r)$ (e/Å^5)	−12.3	−8.8		1.0
ϵ	0.03	0.04		0.02
		TS$_{DF}$		
$\rho_b(r)$ (e/Å^3)	0.44	3.16		0.63
$\nabla^2\rho_b(r)$ (e/Å^5)	1.1	1.3		6.2
ϵ	0.85	0.00		0.19

[a] Based on AIM analysis of B3LYP/6-311+G(2d,p) wave functions.

We now turn to the ring contraction of 3-sila-2-oxacyclohexylidene **A** via the stepwise biradical pathway, involving initial fragmentation via **TS$_{AC}$** to the acyl−silyl biradical **C**, followed by collapse via **TS$_{CD}$** to silacyclopentanone **D** (cf. Scheme 1). The optimized geometric structures for **TS$_{AC}$**, **C**, and **TS$_{CD}$** are shown in Figure 5. Fragmentation of **A** to **C** via **TS$_{AC}$** involves considerable lengthening of the O−Si bond and shortening of the C2−O bond in going from **A** (cf. Figure 1) to **TS$_{AC}$**. This is accompanied by a sizable decrease in $\rho_b(r)$ for the O−Si bond and an increase in $\rho_b(r)$ for the C2−O bond in **TS$_{AC}$** (cf. Table 4) relative to **A** (cf. Table 1). These observations are consistent with O−Si bond fragmentation and C2−O double-bond formation. In the subsequent ring closure of **C** to **D** via **TS$_{CD}$**, the distance between the C2 and Si atoms decreases while that between the O and Si atoms increases in **TS$_{CD}$** relative to **C** (cf. Figure 5), in keeping with C2−Si bond formation and O−Si bond dissociation. We note that the bond length and $\rho_b(r)$ for the C2−O bond remain essentially unchanged in going from **C** to **TS$_{CD}$**, suggesting that C2−O double-bond formation is essentially complete in biradical **C**.

A plot of the Mulliken atomic spin densities for **C** can be found in Figure 8, and AIM atomic spin densities for **TS$_{AC}$**, **C**, and **TS$_{CD}$** are collected in Table 6. From the Mulliken spin densities for **C** in Figure 8, it can be seen that the α spin density is localized on the C2 and O atoms, while the β spin density is

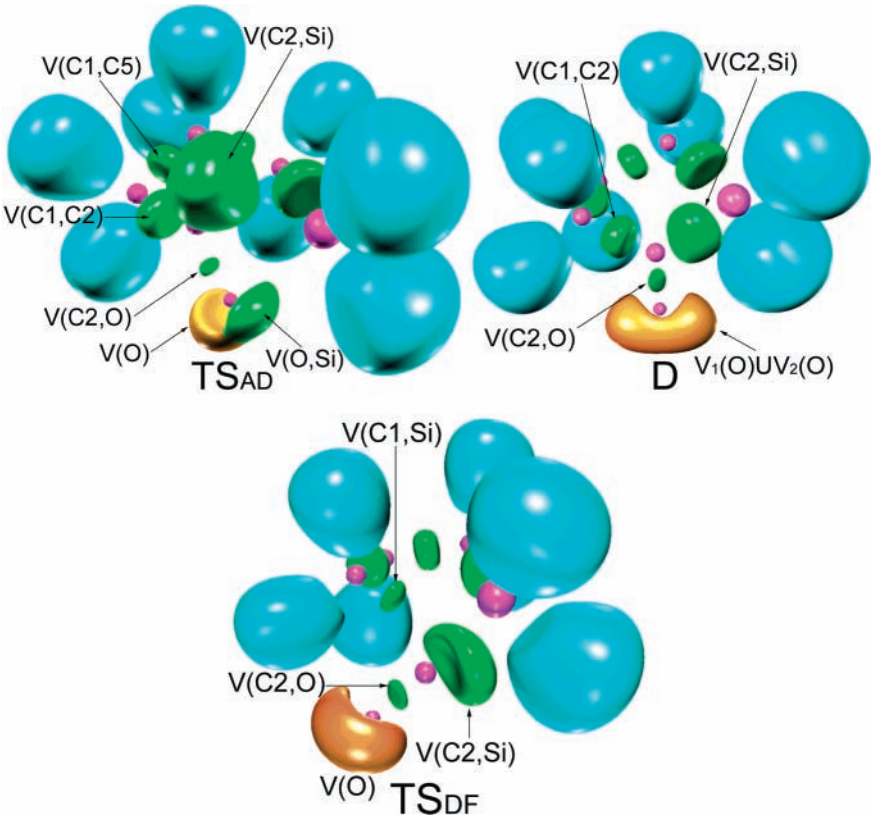

Figure 7. B3LYP/6-311+G(2d,p) ELF isosurfaces for **TS$_{AD}$**, **D**, and **TS$_{DF}$**. The basins shown are core basins (purple), protonated valence basins (blue), disynaptic (bonding) valence basins (green), and monosynaptic (lone-pair) valence basins (orange).

TABLE 5: Average Basin Population $N(\Omega_i)$, Relative Fluctuation $\lambda(\Omega_i)$, and % Cross-Exchange Contribution of TS$_{AD}$, D, and TS$_{DF}$[a]

basin	$N(\Omega_i)$	$\lambda(\Omega_i)$	% cross-exchange contribution[b]
		TS$_{AD}$	
V(C1,C2)	2.03	0.50	V(C2,Si) 9.4; V(C1,H3) 7.9; V(C1,H4) 7.9; V(C1,C5) 6.4
V(C2,O)	1.69	0.60	V(O) 18.9; V(O,Si) 17.8; V(C2,Si) 8.9; V(C1,C2) 5.9
V(C2,Si)	2.32	0.42	V(C1,C2) 8.2; V(C2,O) 6.5; V(O,Si) 5.6; V(O) 3.9
V(O,Si)	2.78	0.48	V(O) 19.4; V(C2,O) 10.8; V(C2,Si) 4.7
V(O)	2.99	0.42	V(O,Si) 18.1; V(C2,O) 10.7; V(C2,Si) 3.0
		D	
V(C1,C2)	1.99	0.51	V(C2,Si) 8.5; V(C1,H3) 8.0; V(C1,H4) 8.0; V(C2,O) 6.5
V(C2,O)	2.30	0.56	V_1(O) 17.4; V_2(O) 16.5; V(C2,Si) 7.4; V(C1,C2) 5.7
V(C2,Si)	2.22	0.45	V(C1,C2) 7.7; V(C2,O) 7.7
V_1(O)	2.55	0.45	V_2(O) 18.0; V(C2,O) 14.9
V_2(O)	2.67	0.44	V_1(O) 17.2; V(C2,O) 15.0
		TS$_{DF}$	
V(C1,Si)	1.30	0.66	V(C2,Si) 13.8; V(C1,C5) 9.2; V(C1,H) 10.8
V(C2,Si)	2.83	0.43	V(C2,O) 9.5; V(O) 8.1; V(C1,Si) 6.4
V(C2,O)	2.64	0.52	V(O) 32.6; V(C2,Si) 10.2
V(O)	4.87	0.30	V(C2,O) 17.7; V(C2,Si) 4.7

[a] Based on ELF analysis of B3LYP/6-311+G(2d,p) wave functions. [b] Contribution of neighboring basins to the total basin population.

almost solely centered on the Si atom. This is supported by the AIM atomic spin densities in Table 6 which show that the α spin density is highest on the C2 and O atoms, while the β spin density is highest on the Si atom. These findings confirm that **C** is indeed an acyl−silyl biradical, with the α and β spin densities primarily localized on the C2 and Si atoms, respectively. It is also evident that the atomic spin densities on the C2, O, and Si atoms increase in going from **A** to **C** via **TS$_{AC}$**, consistent with biradical formation. We also note that in the transition state **TS$_{CD}$** for ring closure of biradical **C** to afford **D**, the α and β spin densities are still largely localized on the C2 and Si atoms, respectively. This localization of spin densities should facilitate C2−Si bond formation and hence ring closure.

Thermochemical data for ring contraction of 3-sila-2-oxacyclohexylidene **A** via the concerted and stepwise biradical pathways can be found in Table 3 and Figure 4. It is evident from these data that ring contraction via the concerted pathway (i.e., via **TS$_{AD}$**) is considerably more favorable than that via the stepwise biradical pathway (i.e., via **TS$_{AC}$**, **C** and **TS$_{CD}$**). Thus, it can be concluded that ring contraction of **A** occurs via a concerted mechanism involving front-side nucleophilic attack by the carbene lone pair at silicon rather than a stepwise mechanism involving the intermediacy of an acyl−silyl biradical.

Decarbonylation. As mentioned earlier, decarbonylation of 3-sila-2-oxacyclohexylidene **A** could involve initial formation

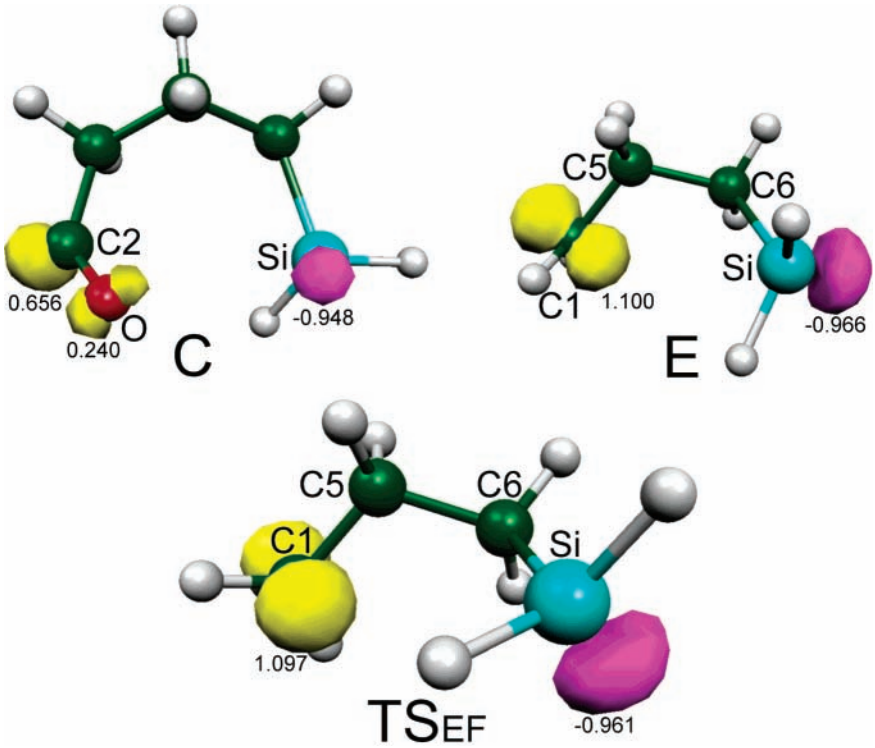

Figure 8. Plots of the B3LYP/6-311+G(2d,p) Mulliken atomic spin densities for **C**, **E**, and $\mathbf{TS_{EF}}$. Positive and negative values denote α and β spin densities, respectively.

TABLE 6: AIM Atomic Spins Densities for $\mathbf{TS_{AC}}$, C, $\mathbf{TS_{CD}}$, $\mathbf{TS_{CE}}$, E, and $\mathbf{TS_{EF}}$[a]

	C1	C2	C5	C6	O	Si
$\mathbf{TS_{AC}}$	0.098	0.522	0.017	−0.048	0.179	−0.613
C	0.115	0.577	0.027	−0.059	0.229	−0.722
$\mathbf{TS_{CD}}$	0.125	0.564	0.010	−0.064	0.248	−0.733
$\mathbf{TS_{CE}}$	0.637	0.174	0.000	−0.059	0.096	−0.740
E	0.873		0.032	0.000		−0.743
$\mathbf{TS_{EF}}$	0.867		0.020	0.034		−0.738

[a] Based on AIM analysis of B3LYP/6-311+G(2d,p) wave functions. Positive and negative values denote α and β spin densities, respectively. Spin densities are taken as the difference between the α and β electron populations, obtained by integration of the spin densities over the atomic basins.

and subsequent decarbonylation of the acyl−silyl biradical **C** to yield the silabutane biradical **E**, which then collapses to silacyclobutane **F** (cf. Scheme 1). Alternatively, decarbonylation could occur via the intermediacy of silacyclopentanone **D** (cf. Scheme 1). We will first consider the former decarbonylation pathway and then focus on the latter. Formation of both **C** and **D** was discussed in the previous sections; in this section, we focus on their decarbonylation. As shown in Scheme 1, decarbonylation of the acyl−silyl biradical **C** via $\mathbf{TS_{CE}}$ affords the silabutane biradical **E**, which then collapses via $\mathbf{TS_{EF}}$ to silacyclobutane **F**. The optimized geometric structures for $\mathbf{TS_{CE}}$, **E**, $\mathbf{TS_{EF}}$, and **F** are shown in Figure 9. For decarbonylation of **C**, considerable lengthening of the dissociating C1−C2 bond and shortening of the developing C2−O triple bond occur in $\mathbf{TS_{CE}}$ relative to **C** (cf. Figure 5). This is accompanied by a significant decrease in $\rho_b(r)$ for the C1−C2 bond and a sizable increase in $\rho_b(r)$ for the C2−O bond in $\mathbf{TS_{CE}}$ relative to **C** (cf. Table 4). Also, the distance between the C2 and Si atoms increases significantly in $\mathbf{TS_{CE}}$ compared to **C** (cf. Figure 5), consistent with the imminent loss of carbon monoxide. We note from the spin densities in Table 6 that there is a considerable shift of the α spin density from the C2 and O atoms to the C1 atom, while the β spin density on the Si atom increases slightly in going from **C** to $\mathbf{TS_{CE}}$ (cf. Table 6), consistent with formation of the silabutane biradical **E** and loss of carbon monoxide.

Now turning to the ring closure of biradical **E**, we note that, in going from **E** to $\mathbf{TS_{EF}}$, the distance between the C1 and Si atoms remains essentially unchanged, while the silyl group rotates significantly about the C6−Si bond, as evidenced by the ∠H8SiC6C5 dihedral angle given in Figure 9. From the plot of the Mulliken spin densities for **E** in Figure 8, it can be seen that the β spin density on Si is oriented away from the α spin density on C1. Thus, it appears that rotation of the silyl group in $\mathbf{TS_{EF}}$ allows interaction between the β spin density on Si and the α spin density on C1 (cf. Figure 8), resulting in C2−Si bond formation and hence ring closure. We also note that there is a slight decrease in the α and β spin densities on C1 and Si, respectively, in $\mathbf{TS_{EF}}$ relative to **E** (cf. Table 7), in accord with ring closure of **E** to afford the closed-shell silacyclobutane **F**.

Let us now consider the mechanism for decarbonylation of silacyclopentanone **D** (cf. Scheme 1). The computed transition-state structure $\mathbf{TS_{DF}}$ is shown in Figure 9. Relative to **D** (cf. Figure 5), considerable lengthening of the dissociating C1−C2 bond and shortening of the developing C2−O triple bond is observed in $\mathbf{TS_{DF}}$, while the distance between the C1 and Si atoms decreases significantly. Surprisingly, though, modest contraction of the dissociating C2−Si bond occurs in $\mathbf{TS_{DF}}$. From the topological properties of the electronic density given in Table 4, it is apparent that $\rho_b(r)$ decreases significantly for the dissociating C1−C2 bond, increases noticeably for the developing C2−O triple bond, and decreases slightly for the dissociating C2−Si bond in $\mathbf{TS_{DF}}$ relative to **D**. Thus, despite the slight C2−Si bond shortening in $\mathbf{TS_{DF}}$, the decrease in $\rho_b(r)$ for the C2−Si bond is clearly indicative of bond dissociation.

Figure 10 contains contour plots of the Laplacian of the electronic density overlaid by bond paths in the C1C2Si plane

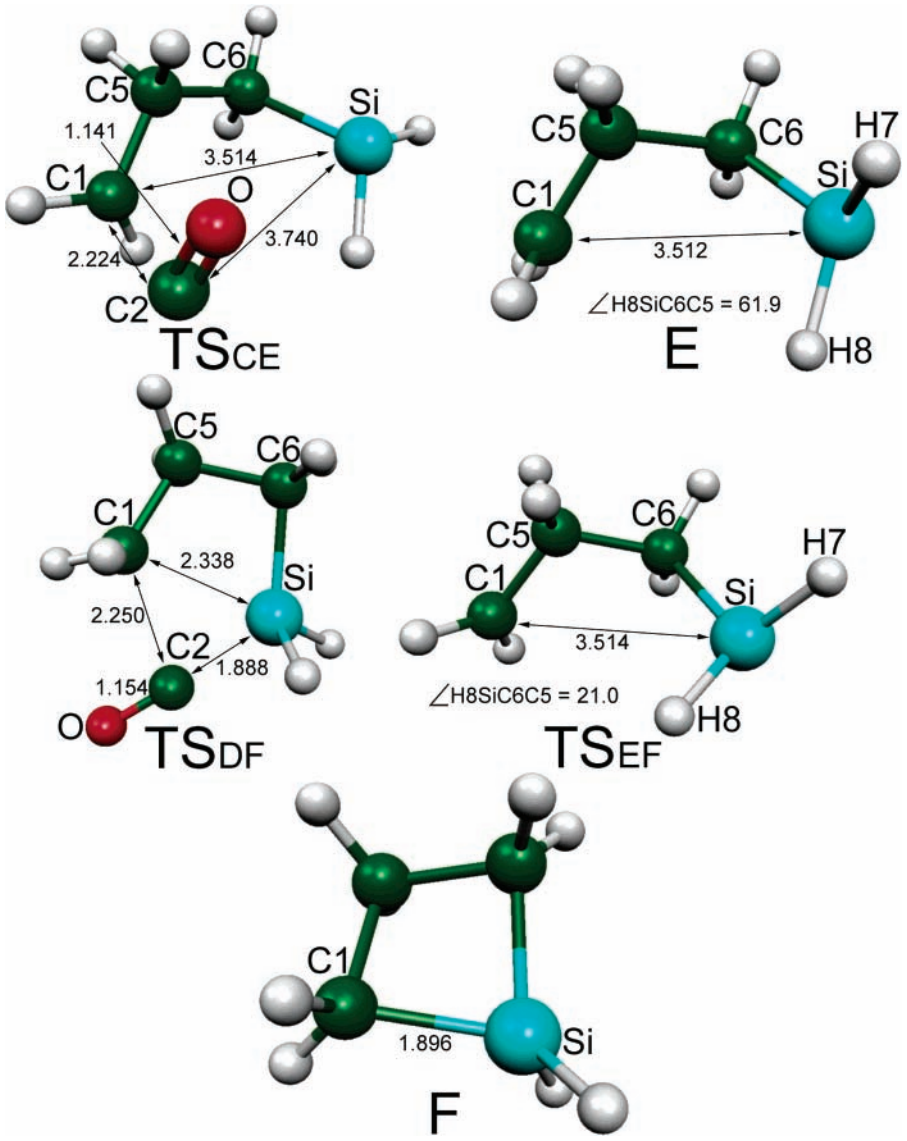

Figure 9. B3LYP/6-311+G(2d,p) optimized molecular geometries for $\mathbf{TS_{CE}}$, **E**, $\mathbf{TS_{DF}}$, $\mathbf{TS_{EF}}$, and **F**. Interatomic distances and dihedral angles are in Å and degrees, respectively.

at selected points along the reaction path for decarbonylation of silacyclopentanone **D**. As mentioned earlier, negative IRC values correspond to the reactant side of the reaction path, positive IRC values correspond to the product side of the reaction path, and an IRC value of zero corresponds to the transition state. From the sequence of plots in the figure, it is apparent that the changes in molecular structure that accompany this reaction occur via a bifurcation mechanism. The plots for IRC = −0.19683 and 0.00000 are in the reactant region of structural stability, while those for IRC = 0.49649 and 0.59648 are in the ring-structure and product regions of structural stability, respectively. The fact that C1−C2 bond cleavage and C1−Si bond formation occurs before complete C2−Si bond dissociation suggests that the electronic density for the C1−Si bond formation primarily results from C1−C2 bond dissociation (cf. Figure 10). This is in keeping with the mechanism for decarbonylation of **D** involving nucleophilic attack by the C1−C2 bonding electrons at silicon (cf. Scheme 1).

ELF isosurfaces for **D** and $\mathbf{TS_{DF}}$ are shown in Figure 7, and corresponding ELF basin properties are collected in Table 5. The disappearance of the V(C1,C2) valence basin and appearance of the V(C1,Si) valence basin in going from **D** to $\mathbf{TS_{DF}}$, together with the fact that the V(C2,Si) basin remains intact, is consistent with C1−C2 bond cleavage and C1−Si bond formation before complete C2−Si dissociation and thus with the mechanism involving nucleophilic attack by the C1−C2 bonding electrons at silicon illustrated in Scheme 1. We note that the V_1(O) and V_2(O) lone-pair valence basins in **D** merge to form a single V(O) lone-pair valence basin in $\mathbf{TS_{DF}}$, which is indicative of C2−O triple-bond formation,[46] a finding further supported by the fact that the population of the V(C2,O) valence basin increases in going from **D** to $\mathbf{TS_{DF}}$. We also note that there is a sizable increase in the V(C2,Si) basin population in $\mathbf{TS_{DF}}$ relative to **D**, most likely as a result of additional cross-exchange contribution from the developing V(C1,Si) basin.

It is not immediately obvious from the thermochemical data in Table 3 and Figure 4 whether decarbonylation of 3-sila-2-oxacyclohexylidene **A** occurs preferentially through the pathway involving initial formation and subsequent decarbonylation of silacyclopentanone **D** via $\mathbf{TS_{AD}}$ and $\mathbf{TS_{DF}}$, respectively, or by the pathway involving initial formation and subsequent decarbonylation of the acyl−silyl biradical **C** via $\mathbf{TS_{AC}}$ and $\mathbf{TS_{CE}}$, respectively, followed by collapse of the silabutane biradical **E** via $\mathbf{TS_{EF}}$ (cf. Scheme 1). Inspection of the Gibbs free-energy profile in Figure 4 reveals that the initial formation of **D** via $\mathbf{TS_{AD}}$ is significantly more favorable than initial formation of

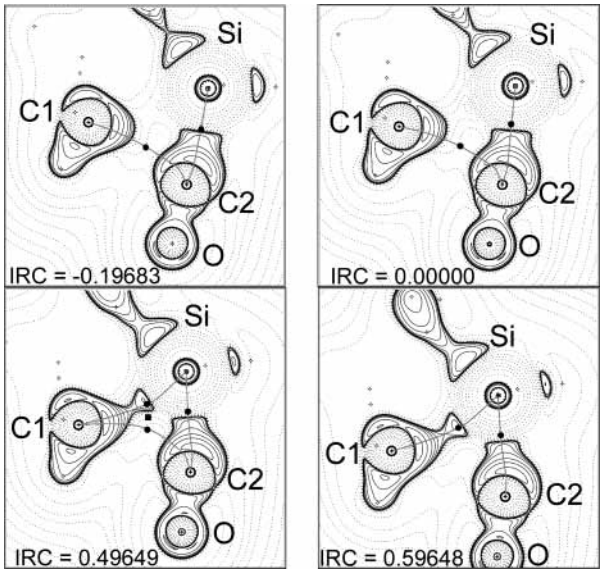

Figure 10. B3LYP/6-311+G(2d,p) contour plots of the Laplacian of the electronic density overlaid by bond paths in the C1C2Si plane at selected IRC values for decarbonylation of silacyclopentanone **D**. Plots for IRC = −0.19683 and 0.00000 amu$^{1/2}$ bohr are in the reactant region of structural stability, while those for IRC = 0.49649 and 0.59648 amu$^{1/2}$ bohr are in the ring-structure and product regions of structural stability, respectively. Solid and broken contours represent regions of charge concentration and charge depletion, respectively, while solid round and square dots identify positions of BCPs and RCPs. Note that some bond paths have deviated out-of-plane.

the acyl−silyl biradical **C** via $\mathbf{TS_{AC}}$. However, the barrier for decarbonylation of thermodynamically stable **D** via $\mathbf{TS_{DF}}$ is considerably larger than that for decarbonylation of **C** via $\mathbf{TS_{CE}}$, **E**, and $\mathbf{TS_{EF}}$. Nevertheless, **C** would more readily revert back to **A** via $\mathbf{TS_{AC}}$ or collapse to **D** via $\mathbf{TS_{CD}}$ than fragment to **E** via $\mathbf{TS_{CE}}$. Thus, it seems most likely that decarbonylation of **A** would preferentially occur via initial formation and subsequent decarbonylation of silacyclopentanone **D** via $\mathbf{TS_{AD}}$ and $\mathbf{TS_{DF}}$, respectively. We note that the same general conclusions can be drawn from inspection of the energy, enthalpy, or free-energy profiles, despite the significant increase in entropy that accompanies fragmentation (decarbonylation) of **C**, which makes the pathway via $\mathbf{TS_{CE}}$, **E**, and $\mathbf{TS_{EF}}$ less favorable in terms of free energies. Overall, 1,2-H migration and ring contraction are significantly more favorable energetically than decarbonylation.

Conclusion

The mechanisms of 1,2-H migration, ring contraction, and decarbonylation of 3-sila-2-oxacyclohexylidene have been investigated using hybrid DFT calculations, the quantum theory of atoms in molecules (AIM), and the electron localization function (ELF). The mechanism for 1,2-H migration was shown to involve a typical hydride-like shift from the migration origin to the "vacant" carbene p orbital, with axial 1,2-H migration being slightly more favorable than its equatorial counterpart. In addition, AIM analysis revealed that the changes in molecular structure associated with this mechanism for 1,2-H migration occur via a *conflict mechanism*. Ring contraction was found to occur via a concerted mechanism involving intramolecular front-side nucleophilic attack by the carbene lone pair at silicon as opposed to a stepwise mechanism involving an acyl−silyl biradical intermediate. In this case, the molecular structure changes that accompany ring contraction occur via a *bifurcation mechanism* according to AIM analysis. Finally, decarbonylation is most likely a stepwise reaction that involves the intermediacy of silacyclopentanone rather than acyl−silyl and alkyl−silyl biradicals. But overall, 1,2-H migration and ring contraction were found to be significantly more favorable energetically than decarbonylation.

Acknowledgment. This work was funded by research grants from the Natural Science and Engineering Research Council of Canada and the Fonds Québécois de Recherche sur la Nature et les Technologies. Calculations were performed at the Centre for Research in Molecular Modeling, which was established with the financial support of the Concordia University Faculty of Arts & Science, the Ministère de l'Éducation du Québec, and the Canada Foundation for Innovation. G.H.P. holds a Concordia University Research Chair.

Supporting Information Available: B3LYP/6-311+G(2d,p) contour plots of the Laplacian of the electronic density for **A** and **B**, as well as topological properties of the electronic density and thermochemical data obtained with the PBE1PBE/6-311+G(2d,p) model chemistry are provided. In addition, Cartesian coordinates and absolute electronic energies for all optimized geometries, as well as imaginary frequencies for the computed transition states and expectation values of the spin operator $\langle S^2 \rangle$ for biradical species, have been supplied. This information is available free of charge via the Internet at http://pubs.acs.org.

References and Notes

(1) Foster, A. M.; Agosta, W. C. *J. Am. Chem. Soc.* **1972**, *94*, 5777.
(2) Foster, A. M.; Agosta, W. C. *J. Am. Chem. Soc.* **1973**, *95*, 608.
(3) Ayral-Kaloustian, S.; Agosta, W. C. *J. Org. Chem.* **1982**, *47*, 284.
(4) Yates, P.; Loutfy, R. O. *Acc. Chem. Res.* **1975**, *8*, 209.
(5) Yates, P.; Tam, J. C. *J. Chem. Soc., Chem. Commun.* **1975**, 737.
(6) Umbricht, G.; Hellman, M. D.; Hegedus, L. S. *J. Org. Chem.* **1998**, *63*, 5173.
(7) Switlak, K.; He, D.; Yates, P. *J. Chem. Soc., Perkin Trans. 1* **1992**, 2579.
(8) Loncke, P. G., Ph.D. Thesis, Concordia University, 2004.
(9) Loncke, P. G.; Gadosy, T. A.; Peslherbe, G. H. *Can. J. Chem.* **2002**, *80*, 302.
(10) Loncke, P. G.; Gadosy, T. A.; Peslherbe, G. H. *Arkivok* **2001**, *2*, 179.
(11) Pezacki, J. P.; Loncke, P. G.; Ross, J. P.; Warkentin, J.; Gadosy, T. A. *Org. Lett.* **2000**, *2*, 2733.
(12) Brook, A. G. *Acc. Chem. Res.* **1974**, *7*, 77.
(13) Brook, A. G.; Pearce, R.; Pierce, J. B. *Can. J. Chem.* **1971**, *49*, 1622.
(14) Duff, J. M.; Brook, A. G. *Can. J. Chem.* **1973**, *31*, 2869.
(15) Hassner, A.; Soderquist, J. A. *Tetrahedron Lett.* **1980**, *21*, 429.
(16) Moss, R. A. In *Advances in Carbene Chemistry*; Brinker, U. H., Ed.; JAI Press Inc.: Greenwich, CT, 1994; Vol. 1, p 59.
(17) Liu, M. T. H. *Acc. Chem. Res.* **1994**, *21*, 287.
(18) Schaefer, H. F. *Acc. Chem. Res.* **1979**, *12*, 288.
(19) Hoffmann, R.; Zeiss, G. D.; Dine, G. W. V. *J. Am. Chem. Soc.* **1968**, *90*, 1485.
(20) Evanseck, J. D.; Houk, K. N. *J. Phys. Chem.* **1990**, *94*, 5518.
(21) Evanseck, J. D.; Mareda, J.; Houk, K. N. *J. Am. Chem. Soc.* **1990**, *112*, 73.
(22) Hoffmann, R.; Woodward, R. B. *Acc. Chem. Res.* **1968**, *1*, 17.
(23) Woodward, R. B.; Hoffmann, R. *Angew. Chem., Int. Ed. Engl.* **1969**, *8*, 781.
(24) Fleming, I. *Frontier Orbitals and Organic Chemical Reactions*; John Wiley & Sons: Ltd.: Chichester, 1976.
(25) Fukui, K. *Science* **1982**, *218*, 747.
(26) Rauk, A. *Orbital Interaction Theory of Organic Chemistry*, 2nd ed.; Wiley-Interscience: New York, 2001.
(27) Gilchrist, T. L.; Storr, R. C. *Organic Reactions and Orbital Symmetry*, 2nd ed.; Cambridge University Press: London, 1979.
(28) Selection rules for 1,2-sigmatropic rearrangements also indicate that this rearrangement mechanism is *symmetry forbidden* since it involves a four-electron (or 4*n*) antiaromatic transition state. For similar rearrangements in carbanions, see, e.g., Grovenstein, *Angew. Chem., Int. Ed. Engl.* **1978**, *17*, 313.
(29) Becke, A. D. *J. Chem. Phys.* **1993**, *98*, 5648.

(30) Jensen, F. *Introduction to Computational Chemistry*; John Wiley & Sons Ltd.: Baffins Lane, 1999.

(31) Lee, C.; Yang, W.; Parr, R. G. *Phys. Rev. B* **1988**, *37*, 785.

(32) Mixing the HOMO and LUMO results in a singlet wave function in which $\langle S^2 \rangle$ is greater than 0 due to contributions from triplet and higher-lying electronic states. While this is indicative of a spin-contaminated wave function in wave-function-based theory, this is not necessarily the case in DFT (Cremer et al. *Int. J. Mol. Sci.* 2002, 3, 360). Since single-determinant DFT calculations on open-shell singlet biradicals often collapse to the closed-shell solutions (i.e., $\langle S^2 \rangle = 0$), we checked to make sure that $\langle S^2 \rangle$ is greater than 0 to ensure that we did indeed obtain the open-shell solutions.

(33) Grafenstein, J.; Kraka, E.; Filatov, M.; Cremer, D. *Int. J. Mol. Sci.* **2002**, *3*, 360.

(34) Perdew, J. P.; Burke, K.; Ernzerhof, M. *Phys. Rev. Lett.* **1996**, *77*, 3865.

(35) Perdew, J. P.; Ernzerhof, M.; Burke, K. *J. Chem. Phys.* **1996**, *105*, 9982.

(36) Perdew, J. P.; Burke, K.; Ernzerhof, M. *Phys. Rev. Lett.* **1997**, *78*, 1396.

(37) Frisch, M. J.; Trucks, G. W.; Schlegel, H. B.; Scuseria, G. E.; Robb, M. A.; Cheeseman, J. R.; Zakrzewski, V. G.; Montgomery, J. A., Jr.; Stratmann, R. E.; Burant, J. C.; Dapprich, S.; Millam, J. M.; Daniels, A. D.; Kudin, K. N.; Strain, M. C.; Farkas, O.; Tomasi, J.; Barone, V.; Cossi, M.; Cammi, R.; Mennucci, B.; Pomelli, C.; Adamo, C.; Clifford, S.; Ochterski, J.; Petersson, G. A.; Ayala, P. Y.; Cui, Q.; Morokuma, K.; Malick, D. K.; Rabuck, A. D.; Raghavachari, K.; Foresman, J. B.; Cioslowski, J.; Ortiz, J. V.; Stefanov, B. B.; Liu, G.; Liashenko, A.; Piskorz, P.; Komaromi, I.; Gomperts, R.; Martin, R. L.; Fox, D. J.; Keith, T.; Al-Laham, M. A.; Peng, C. Y.; Nanayakkara, A.; Gonzalez, C.; Challacombe, M.; Gill, P. M. W.; Johnson, B. G.; Chen, W.; Wong, M. W.; Andres, J. L.; Head-Gordon, M.; Replogle, E. S.; Pople, J. A. *Gaussian 98*, revision A.11.4; Gaussian, Inc.: Pittsburgh, PA, 1998.

(38) Schlegel, H. B. *J. Comput. Chem.* **1982**, *3*, 214.

(39) Bannerjee, A.; Adams, N.; Simons, J.; Shepard, R. *J. Phys. Chem.* **1985**, *89*, 52.

(40) Simons, J.; Jorgensen, P.; Taylor, H.; Ozment, J. *J. Phys. Chem.* **1983**, *87*, 2745.

(41) Cerjan, C. J.; Miller, W. H. *J. Chem. Phys.* **1981**, *75*, 2800.

(42) Ochterski, J. W. *Thermochemistry in Gaussian*; Gaussian Inc.: Pittsburgh, PA, 2000.

(43) Bader, R. F. W. *Atoms in Molecules. A Quantum Theory*; Clarendon Press: Oxford, 1990.

(44) Becke, A. D.; Edgecombe, K. E. *J. Chem. Phys.* **1990**, *92*, 539.

(45) Silvi, B.; Savin, A. *Nature* **1994**, *371*, 683.

(46) Savin, A.; Nesper, R.; Wengert, S.; Fassler, T. *Angew. Chem., Int. Ed. Engl.* **1997**, *36*, 1809.

(47) Noury, S.; Colonna, F.; Savin, A.; Silvi, B. *J. Mol. Struct.* **1998**, *450*, 59.

(48) Savin, A.; Silvi, B.; Colonna, F. *Can. J. Chem.* **1996**, *74*, 1088.

(49) The AIMPAC suite of programs is available from Professor R. F. W. Bader, McMaster University, Canada and from the AIMPAC website (www.chemistry.mcmaster.ca/aimpac).

(50) Biegler-Konig, F. W.; Bader, R. F. W.; Tang, T. *J. Comput. Chem.* **1982**, *3*, 317.

(51) Biegler-König, F.; Schönbohm, J.; Bayles, D. *J. Comput. Chem.* **2001**, *22*, 545.

(52) Noury, S.; Krokidis, X.; Fuster, F.; Silvi, B. *TopMod Package*; Université Pierre et Marie Curie: Paris, 1997.

(53) SciAn is a free scientific visualization and animation program for high-performance graphic workstations developed by E. Pepke, J. Murray, J. Lyons, and Y. Hwu that can be obtained from the CCL website (www.ccl.net/cca/software/AIX/index.shtml).

(54) Reed, A. E.; Curtiss, L. A.; Weinhold, F. *Chem. Rev.* **1988**, *88*, 899.

(55) Glendening, E. D.; Reed, A. E.; Carpenter, J. E.; Weinhold, F. *NBO 3.0 Program Manual*; Theoretical Chemistry Institute and Department of Chemistry, University of Wisconsin: Madison, Wisconsin.

(56) Sulzbach, H. M.; Platz, M. S.; Schaefer, H. F.; Hadad, C. M. *J. Am. Chem. Soc.* **1997**, *119*, 5682.

(57) Evanseck, J. D.; Houk, K. N. *J. Am. Chem. Soc.* **1990**, *112*, 9148.

(58) Kyba, E. P.; John, A. M. *J. Am. Chem. Soc.* **1977**, *99*, 8329.

(59) Press, L. S.; Shechter, H. *J. Am. Chem. Soc.* **1979**, *101*, 509.

(60) Kyba, E. P. *J. Am. Chem. Soc.* **1977**, *99*, 8330.